REPORT SD-TR-89-43

(4)

The Auroral Energy Depostion Over the Polar Ionosphere During Substorms

B.-H. AHN
Cooperative Institute for Research in Environmental Sciences
University of Colorado
Boulder, CO 80309-0449

H. W. KROEHL
National Geophysical Data Center
Boulder, CO 80303

Y. KAMIDE
Kyoto Sangyo University
Kyoto 603, Japan

D. J. GORNEY
Laboratory Operations
The Aerospace Corporation
El Segundo, CA 90245-4691

S.-I. AKASOFU and J. R. KAN
Geographical Institute
University of Alaska
Fairbanks, AL 99775-0800

15 June 1989

Prepared for

SPACE SYSTEMS DIVISION
AIR FORCE SYSTEMS COMMAND
Los Angeles Air Force Base
P.O. Box 92960
Los Angeles, CA 90009-2960

This report was submitted by The Aerospace Corporation, El Segundo, CA 90245, under Contract No. F04701-85-C-0086-P00019 with the Space Systems Division, P.O. Box 92960, Los Angeles, CA 90009-2960. It was reviewed and approved for The Aerospace Corporation by H. R. Rugge, Director, Space Sciences Laboratory.

Lt Tyron Fisher was the project officer for the Mission-Oriented Investigation and Experimentation (MOIE) Program.

This report has been reviewed by the Public Affairs Office (PAS) and is releasable to the National Technical Information Service (NTIS). At NTIS, it will be available to the general public, including foreign nationals.

This technical report has been reviewed and is approved for publication. Publication of this report does not constitute Air Force approval of the report's findings or conclusions. It is published only for the exchange and stimulation of ideas.

TYRON FISHER, 2LT, USAF
MOIE Project Officer
SSD/CLFPO

JAMES A. BERES, LT COL, USAF
MOIE Program Manager
AFSTC/WCO OL-AB

REPORT DOCUMENTATION PAGE

1a. REPORT SECURITY CLASSIFICATION Unclassified	1b. RESTRICTIVE MARKINGS
2a. SECURITY CLASSIFICATION AUTHORITY	3. DISTRIBUTION/AVAILABILITY OF REPORT Approved for public release; distribution unlimited.
2b. DECLASSIFICATION/DOWNGRADING SCHEDULE	
4. PERFORMING ORGANIZATION REPORT NUMBER(S) TR-0088(3940-06)-8	5. MONITORING ORGANIZATION REPORT NUMBER(S) SD-TR-89-43
6a. NAME OF PERFORMING ORGANIZATION The Aerospace Corporation Laboratory Operations 6b. OFFICE SYMBOL (If applicable)	7a. NAME OF MONITORING ORGANIZATION Space Systems Division
6c. ADDRESS (City, State, and ZIP Code) El Segundo, CA 90245	7b. ADDRESS (City, State, and ZIP Code) Los Angeles Air Force Base Los Angeles, CA 90009-2960
8a. NAME OF FUNDING/SPONSORING ORGANIZATION 8b. OFFICE SYMBOL (If applicable)	9. PROCUREMENT INSTRUMENT IDENTIFICATION NUMBER F04701-85-C-0086-P00019
8c. ADDRESS (City, State, and ZIP Code)	10. SOURCE OF FUNDING NUMBERS PROGRAM ELEMENT NO. / PROJECT NO. / TASK NO. / WORK UNIT ACCESSION NO.

11. TITLE (Include Security Classification)
The Auroral Energy Deposition over the Polar Ionosphere during Substorms

12. PERSONAL AUTHOR(S)
Ahn, B. -H. (University of Colorado), Kroehl, H. W. (National Geophysical Data Center),

13a. TYPE OF REPORT	13b. TIME COVERED	14. DATE OF REPORT (Year, Month, Day)	15. PAGE COUNT
	FROM _____ TO _____	1989 June 15	42

16. SUPPLEMENTARY NOTATION

17. COSATI CODES			18. SUBJECT TERMS (Continue on reverse if necessary and identify by block number)
FIELD	GROUP	SUB-GROUP	aurora, substorms, ionosphere, remote sensing

19. ABSTRACT (Continue on reverse if necessary and identify by block number)

The global Joule heating distributions for the period of July 23-24, 1983, are estimated through the magnetogram inversion method developed by Kamide et al. (1981). Unlike previous works, which mostly used one of the statistically determined conductance models, this study employs instantaneous ionospheric conductance distributions deduced from the DMSP-F6 bremsstrahlung X-ray image data. Also estimated from the X-ray data are instantaneous global particle heating distributions.

The two heating distributions thus obtained allow us to investigate various aspects of heat energy processes over the polar ionosphere on an instantaneous basis. A special emphasis is placed on their spatial and temporal behaviors. Several important results of this study are summarized as follows: (1) Regions of significant Joule heating are closely associated with

20. DISTRIBUTION/AVAILABILITY OF ABSTRACT	21. ABSTRACT SECURITY CLASSIFICATION
☒ UNCLASSIFIED/UNLIMITED ☐ SAME AS RPT. ☐ DTIC USERS	Unclassified

22a. NAME OF RESPONSIBLE INDIVIDUAL	22b. TELEPHONE (Include Area Code)	22c. OFFICE SYMBOL

12. PERSONAL AUTHORS (Continued)

Kamide, Y. (Kyoto Sangyo University), Gorney, D. J. (The Aerospace Corporation), Akasofu, S. -I, and Kan, J. R. (University of Alaska)

19. ABSTRACT (Continued)

the auroral electrojets prominently in the dawn and dusk sectors. (2) The major Joule heating usually occurs poleward of the major particle heating region, particularly in the morning sector. On the other hand, the two heating patterns are complementary in the longitudinal direction. (3) There is a higher correlation between the global Joule heating rate (U_J) and AE(12) than between the global particle heating rate (U_A) and AE(12). (4) The particle heating rate tends to be more prominent during the maximum phase of substorms and afterward than during the pre-expansion phase. (5) The U_J/U_A ratio varies by more than a factor of 10, suggesting the wide variability in the relative importance of the two heating rates. On the average, however, U_J is larger than U_A by a factor of 6.

PREFACE

We acknowledge the generous hospitality of NOAA's National Geophysical Data Center and partial support from the Korea Science and Engineering Foundation.

CONTENTS

FIGURES

1. Introduction

The auroral energy dissipation over the polar ionosphere in the forms of Joule heat dissipation and particle precipitation during magnetospheric substorms is one of the central problems in the study of magnetosphere-ionosphere-thermosphere coupling. To monitor these important quantities, various techniques have been utilized, including satellite and incoherent scatter radar measurements (Wickwar et al., 1975; Brekke, 1976; Banks et al., 1981; Wallis and Budzinski, 1981; Spiro et al., 1982; Vickrey et al., 1982; Foster et al., 1983, 1986; Fuller-Rowell and Evans, 1987; Hardy et al., 1987; Lummerzheim, 1987) and the so-called magnetogram-inversion algorithm (Kamide et al., 1982, 1983, 1986; Ahn et al., 1983; Baumjohann and Kamide, 1984; Richmond et al., 1988). Satellite and radar data are indeed invaluable in that they provide direct measurement of these quantities, but the presently available facilities do not have sufficient spatial coverage to provide instantaneous patterns of the global energy dissipation on a continuous basis. On the other hand, the magnetogram-inversion methods have an advantage over the more direct techniques in offering greater spatial coverage for a given instant as well as high time resolution (say, 5 minutes), although the results are indirect. As pointed out by Kamide and Richmond (1982), the electric potential distribution, from which the Joule heating rate is calculated, is seriously affected by the choice of ionospheric conductance models. Also, the particle heating rate cannot be estimated with this indirect technique, although an attempt (Ahn et al., 1983) has been made to obtain an empirical relation using Chatanika radar measurements of the particle heating rate and ground magnetic disturbances at College, Alaska.

In spite of such limitations of the magnetogram-inversion method, a large number of studies about the Joule heating rate have been made by employing statistically constructed conductance models.

Recently, information on precipitating electron spectra has been available through bremsstrahlung X-ray data from satellite measurements (see Imhof et al., 1974, 1988; Mizera et al., 1978, 1984, 1985). This two-dimensional information about precipitating particles makes it possible to estimate the corresponding global particle heating rate. Furthermore, this technique provides an opportunity to obtain a realistic global conductance distribution, which, in turn, allows one to monitor a realistic global Joule heating rate through the magnetogram-inversion method.

The purpose of this report is to set parameters for the global Joule and particle heating rates in terms of geomagnetic indices, thus providing an important input parameter for the study of energy coupling between the solar wind and the magnetosphere and thermospheric dynamics. Furthermore, such information will be useful in estimating the total energy dissipation in the polar ionosphere.

2. Data and Procedure

Ground magnetometer data from a total of 88 stations in the northern hemisphere during the period July 23-24, 1983, are used in this study; for a list of stations, and their locations, see Ahn et al. (1988). The two-day interval was chosen for study because of continuous data availability and because the period is characterized by intense magnetic activities in the polar

region. The first substorm activity on July 23 peaked at 0905 UT and lasted for several hours. Later, magnetic activity soon increased gradually, and a period of almost continuous magnetic disturbances persisted until about 0800 UT on July 24. A series of substorms occurred during the rest of the day. The top and second panels of Figure 1 show the IMF B_z component and the AE(12) index, respectively, during the two-day interval.

The precipitating electron spectrum was inferred from the bremsstrahlung X-ray image data obtained from the DMSP-F6 satellite (see, for example, Rosenberg et al., 1987) by a numerical optimization scheme, which computes the electron spectral shape such that it is most consistent with the observed X-ray energy spectrum. Moreover, it can be determined quite accurately, since the transfer function between the precipitating electron flux and the bremsstrahlung X-ray flux is well known. While the X-ray technique has a great advantage over the other method in estimating the large-scale precipitating electron spectral parameters, there are several drawbacks inherited from the orbital characteristics of the satellite and the sensitivity of the instrument on board. First, the X-ray technique is inherently indirect because of the required numerical conversion from X-ray energy to precipitating electron energy. Second, an X-ray image over the polar region is obtained only every 101 minutes, corresponding to the orbital period of the satellite. Between 15 and 17 minutes are required to scan the complete polar region. Fortunately, a marked auroral conjugacy between the northern and southern hemispheres (Akasofu, 1977, and references therein; Mizera et al., 1987) makes it possible to use the images taken over both the northern and southern polar regions, thus providing an updated image about every 50 minutes. Further, the AE(12) indices shown in Figure 1 are averaged over 17 minutes,

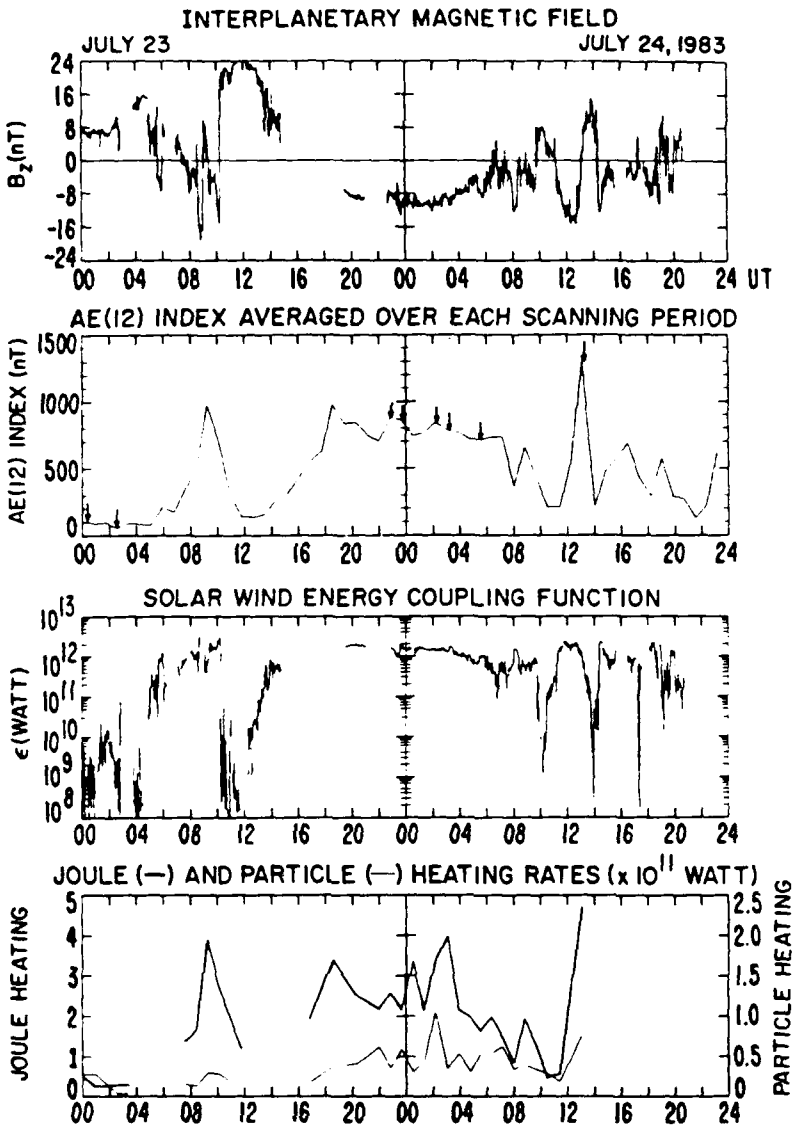

Figure 1. The Top Panel Shows the IMF B_z Component on July 23 and 24, 1983. The AE(12) index shown in the second panel is averaged over each scanning period of the satellite, regardless of data availability of the X-ray image, thus erasing the impulsive nature of the index. The third panel shows the solar wind energy coupling function ε. The bottom panel shows the globally integrated Joule (U_J) and particle (U_A) heating rates for 30 epochs during which the X-ray image data were available. The thick and thin traces represent the global Joule and particle heating variations, respectively. Note two different scales are used for easy comparison.

the scanning period of the satellite. That imposes a serious limitation for the study of temporal aspects of substorm dynamics. Third, the low-altitude satellite could cover the field of view of only about 3000 km. Furthermore, due to the tilt of the geomagnetic axis to the rotational axis and the inclination of the satellite (99°), quite often a significant portion of the auroral zone is out of the field of view. Thus, whenever needed, data manipulation has been performed to fill up the data gap; for details, see Ahn et al. (1988). Another weak point of the X-ray remote-sensing technique is its relative insensitivity to electrons at energies less than 1.5 keV. However, the exclusion of the low-energy portion of the spectrum does not significantly affect our estimations of the total electron energy flux and conductance distribution (e.g., Strickland et al., 1983). With these limitations in mind, we estimated the particle heating rate (U_A) (ergs/cm^2·sec) at each grid point, spaced 1° in latitude and 15° in longitude from the pole to 50°, thus dividing the entire polar region into 960 cells. By integrating the entire polar region with the assumption that the heating rate is constant within each cell and represented by the value at the center of the cell, we obtained the global particle heating rate (U_A).

The Hall and Pedersen conductances are estimated through the empirical formula

$$\sum_P = \left(\frac{20E_0}{4 + E_0^2}\right)\psi^{1/2}$$

$$\frac{\sum_H}{\sum_P} = (E_0)^{5/8}$$

where E_0 is the average electron energy in keV, ψ is the energy flux in ergs · cm^{-2} sec^{-1}, and $\sum_P$ and $\sum_H$ stand for the Pedersen and Hall conductances in

mhos, respectively (e.g., Spiro et al., 1982). Other similar relationships between participating electron spectral parameters and ionospheric conductance have been proposed (e.g., Robinson et al., 1987), but the differences between these relationships and that which was used are not significant for their study. In order to complete the ionospheric conductance distribution, the "background" conductance of solar UV origin is added, using the model proposed by Kamide and Matsushita (1979).

Given the ionospheric conductance distribution, an electric potential distribution can be calculated through magnetogram inversion techniques using ground magnetic data as input. In this study, an improved version of the so-called KRM algorithm by Kamide et al. (1981) is employed. Once the electrostatic potential (Φ) is determined, the Joule heating rate (U_J) is obtained, as follows:

$$u_J = \underline{I_P} \cdot \underline{E} = \Sigma_P \cdot E^2 = \Sigma_P \cdot (-\nabla\Phi)^2,$$

where E stands for the electric field. We calculated u_J at every grid point over the entire polar region, as well as the global heating rate (U_J). In this case, the integration was performed down to 50°, since the contribution of the Joule heating at mid- and low-latitudes is negligible (Ahn et al., 1983). Both the Joule and particle heating rates are obtained altogether for 30 epochs, for which X-ray image data were available.

3. Resul

In this section, we examine the two energy dissipation modes in the polar ionosphere on an individual basis. Figures 2 and 3 show the distributions of the ionospheric current vectors, Joule heating, and particle heating for eight

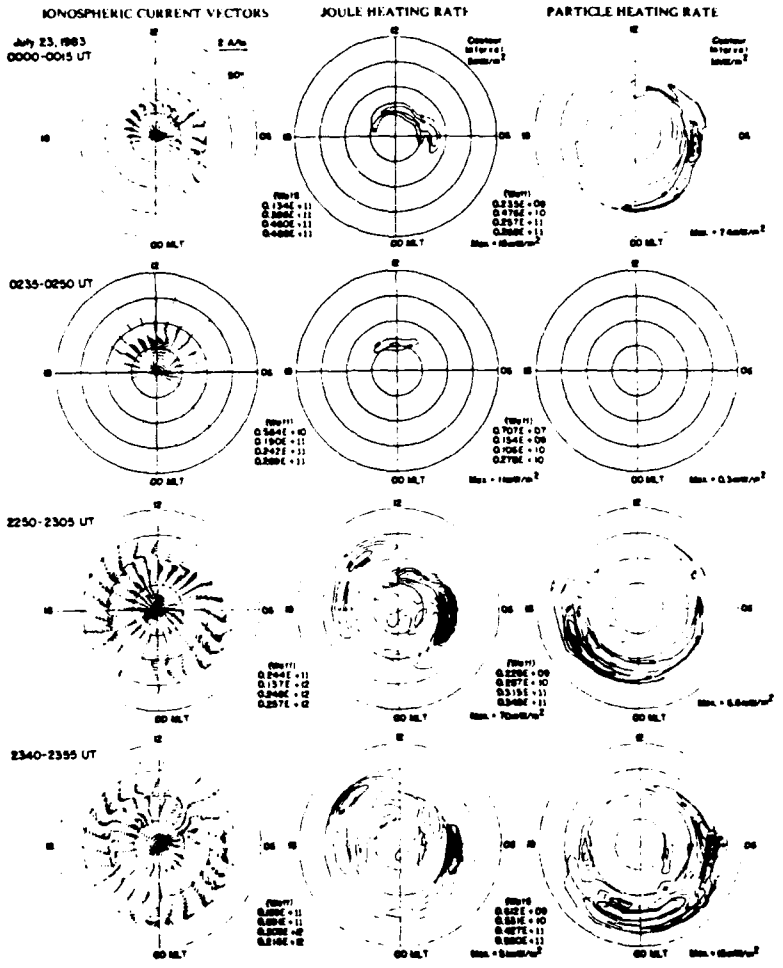

Figure 2. The Distributions of the Ionospheric Current, Joule Heating, and Particle Heating, Plotted in a Magnetic Latitude/Local-Time Reference Frame for the Epochs of 0000-0015 UT, 0235-0250 UT, 2250-2305 UT, and 2340-2355 UT, on July 23, 1983. The latitude circles mark latitudes of 80°, 70°, 60°, and 50°. The outermost contour levels in the Joule and particle heating distributions are 5 and 1 mW/m^2, respectively, and the adjacent contours are drawn at 5 mW/m^2 for Joule and 1 mW/m^2 intervals for particle heating rate. The quantity shown in the lower-right corner of each distribution depicts the maximum heating rate in mW/m^2. Also shown in the left-bottom are the integrated heating rates from the pole to 80°, 70°, 60°, and 50° in watts.

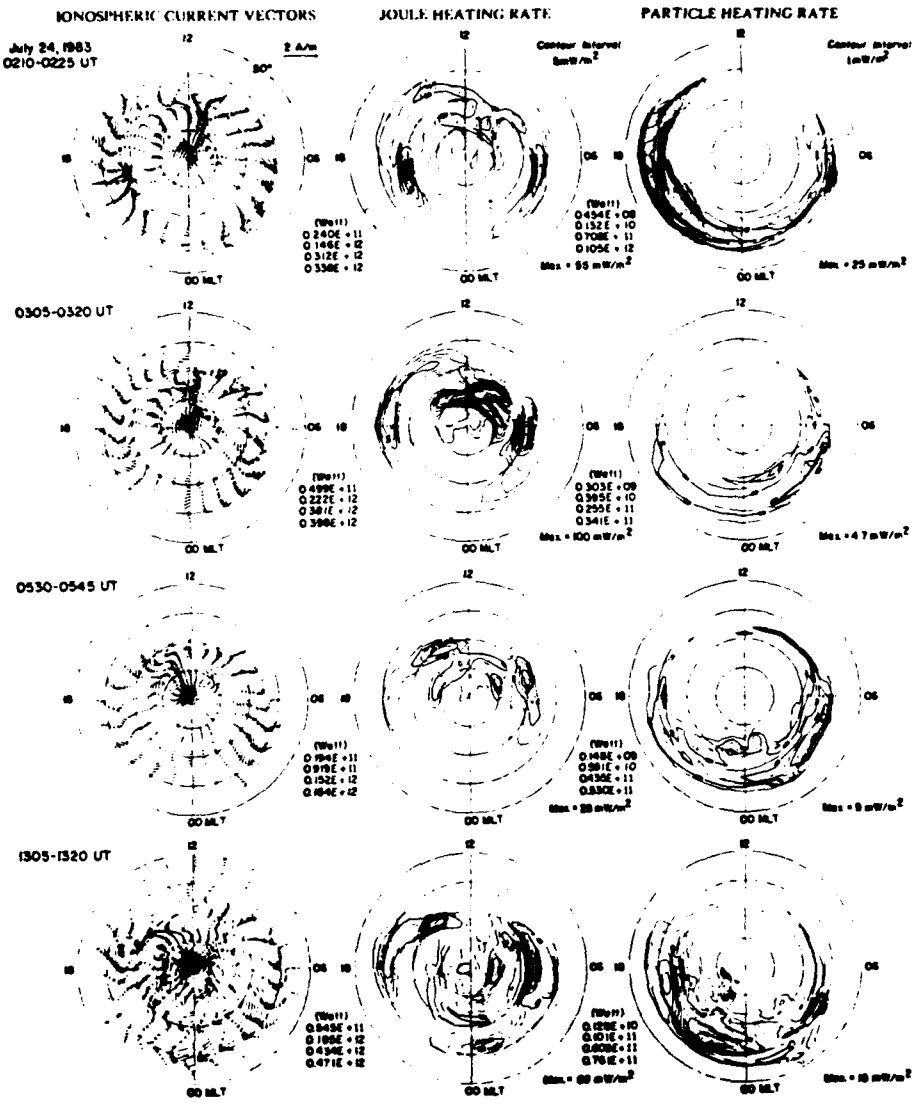

Figure 3. Same as Figure 2 for the Epochs of 0210-0225 UT, 0305-0320 UT, 0530-0545 UT, and 1305-1320 UT on July 24, 1983

epochs during the two-day interval. The first two epochs, 0000-0015 UT and 0235-0250 UT on July 23, 1983, shown in Figure 2, represent a quiet period. The next five epochs, from 2250 UT on July 23 to 0545 UT on July 24, shown partly in Figure 2 and partly in Figure 3, spanned a period of continuous substorm activity. The last epoch, shown in Figure 3, represents the most intense substorm that occurred during the two-day interval. For the purpose of demonstrating the substorm development, the distribution of ionospheric current vectors is included for all epochs examined in this study, since the intensification of the auroral electrojets, and particularly the location of the leading edge of the westward electrojet, are closely associated with the substorm phases (Kamide, 1982; Kamide et al., 1986; Ahn et al., 1984).

The outermost contours of the distributions of the Joule and particle heating rates are 5 mW/m^2 and 1 mW/m^2, respectively, and contours are drawn at 5 mW/m^2 intervals for Joule heating and at 1 mW/m^2 intervals for the particle heating rate. The maximum heating rate of each distribution is given in the lower-right corner in units of mW/m^2. In addition, the globally integrated heating rates from the pole to 80°, 70°, 60°, and 50° in latitude are also shown in the lower-left corner in units of watts. The bottom panel of Figure 1 presents the globally integrated heating rates of the two energy dissipation modes for one hemisphere for the 30 epochs. Note that the scale value of the particle heating rate is enlarged twice for easy comparison. The solar wind energy coupling function ϵ (Perreault and Akasofu, 1978; Akasofu, 1981) during the two-day period is also shown in Figure 1.

a. 0000-0250 UT on July 23

During the epoch at 0000-0015, shown in the top panel of Figure 2, a significant current flow is found primarily in the dayside cusp region, with very weak signature of the westward electrojet in the postmidnight quadrant and of the eastward electrojet in the early evening sector. Also noticeable is an eastward current flow stretched from the early morning to noon sectors along the equatorward boundary of the westward electrojet. Such a flow pattern was identified as a quiet-time character by Ahn et al. (1984). Furthermore, the pattern is quite similar to the one suggested by Friis-Christensen et al. (1985) for IMF conditions of positive B_z and nearly null B_y. The prominent feature of the Joule heating distribution is an enhanced strip associated with strong current flow in the dayside cusp region, while the particle heating pattern is characterized by significant energy deposition along the auroral oval in the entire morning hemisphere.

The situation for two and one-half hours later is shown in the second panel of Figure 2. The magnetic activity has further decreased during the period, with the AE(12) index registering as low as 87 nT, while the IMF B_z component showed a large positive trend. The ionospheric current distribution pattern clearly reflects such a reduced geomagnetic condition. As expected from the magnetic activity, the Joule heating distribution exhibits the same characteristics as before, but the heating rate reduced by a factor of 2. On the other hand, a drastic change occurred in the particle heating distribution; that is, the global heating rate decreased by as much as a factor of 10 compared to the previous epoch. Furthermore, the maximum heating rate was even lower than the lowest

contour level, 1 mW/m^2. It is interesting to point out that this drastic decrease in the particle heating rate occurred during a period in which the magnetic activity in terms of the AE(12) index decreased only about 20 nT from the level of under 100 nT. Although it is not shown in Figure 1, the two and one-half hour interval followed an intense substorm, which maximized at about 2230 UT on July 22, suggesting perhaps that the two cases examined here might, in fact, be during the late recovery phase of a substorm. If that is indeed the case, the electric field strength that is largely responsible for the Joule heating seems to decrease much more slowly than does the intensity of particle precipitation.

b. 2250 UT on July 23-0545 UT on July 24

After having attained a large positive value at about 1200 UT on July 23, the IMF B_Z component began to switch gradually southward and reached a more or less stable period with a large southward component of about -10 nT. Although there were several hour-long data gaps, such a stable southward IMF condition seems to persist for more than 6 hours. The five epochs chosen for examination here roughly coincide with this period. Before examining them, several interesting features observed during the preceding epochs but not selected as examples for discussion deserve brief mention.

Due to a large data gap of the IMF after about 1500 UT on July 23, it is difficult to determine at which moment the IMF turned southward. However, the steady increase in magnetic activity in terms of the AE(12) index indicates that there was a continuous energy input from the solar wind during the period. Note that the AE(12) index at about 1600 UT on July 23 registered as high as 400 nT

without any significant X-ray fluxes, suggesting that the intensity of the precipitating electrons at energies above 1 keV was well under the threshold value of the X-ray detector. This indicates that the enhancement of the electric field seems to be more important than the enhancement of the ionospheric conductance for the high geomagnetic activity during that period. In contrast, the opposite trend of a significant particle precipitation without accompanying any appreciable enhancement of the AE index occurred during the epoch at 0000-0015 UT on July 23, which is considered as the recovery phase of an intense substorm. Appreciable particle heating began only at about 1650 UT. Unfortunately, the IMF data gap during the period and the limited time resolution of the image data prevent us from relating the onset of appreciable particle precipitation with the IMF variation.

The ionospheric current distribution at 2250-2305 UT on July 23 shows well-developed auroral electrojets, which are closely associated with the major Joule heating regions except for the late evening and local midnight sectors where no significant heating was present. Such characteristics of the heating pattern have also been reported from the Chatanika radar measurements (Banks, 1977; Vickrey et al., 1982). On the other hand, the particle heating occurred mostly over an oval-shaped region with the globally integrated heating rate being 3.5×10^{10} watts, corresponding to 13.5% of the global Joule heating rate. A comparison of the spatial relationship of the two heating modes reveals interesting aspects. First, the regions of appreciable particle heating are located generally equatorward of the major Joule heating regions, particularly in the morning sector. Second, the particle heating is intense in the premidnight

quadrant, where the Joule heating is relatively unimportant. Thus, the entire auroral latitude is a region of strong energy deposition due to the complementary longitudinal distribution of Joule heating and particle heating.

The ionospheric current distribution during the period 2340-2355 UT on July 23 shows more disturbed signatures than were present 50 minutes earlier. Notice that the auroral electrojets, particularly the leading edge of the westward electrojet in the midnight sector, expanded equatorward and intruded into the evening sector, indicating that this epoch was during the maximum phase of a substorm (Kamide, 1982; Ahn et al., 1984). In spite of such a dramatic growth of the midnight auroral electrojet, the Joule heating distribution pattern of this epoch is basically the same as that of the previous epoch, with the two major heating regions centered in evening and morning hours. Interestingly, both the global heating and the maximum heating rates decreased more than 15% compared to the previous epoch.

On the other hand, significant changes occurred within the 50 minute period in the particle heating rate, both in the magnitude and its distribution pattern. The global particle heating rate (U_A) increased by a factor of almost 2 over the previous epoch. These changes in the distribution pattern are characterized by the expansion of the major heating regions, both in the equatorward and poleward directions and their shift from the evening sector to the postmidnight quadrant. The particle heating seems to be significant only during the maximum phase of substorms and to have more pronounced local structures than does the Joule heating distribution.

During this prolonged southward IMF period, there were several electrojet intensifications. The epoch 0210-0225 UT on July 24 is during one such period. The ionospheric current distribution of this epoch, shown in Figure 3, clearly exhibits the signature of the maximum phase with the deep intrusion of the westward electrojet into the evening sector along the poleward boundary of the eastward electrojet. As expected, the overall features of the Joule heating distribution are quite similar to those of the two previous examples, with some additional enhancements in the noon and early evening sectors. Again, no significant Joule heating is found in the midnight sector.

The particle heating distribution of this epoch in Figure 3 is characterized by a very strong energy deposition along the auroral oval on the dusk side. The global particle heating rate (U_A) registered about 1 x 10^{11} watts, the highest rate during the two-day interval, although it is not the most disturbed epoch in terms of the AE(12) index. The maximum heating region in the evening sector is probably associated with a westward traveling surge. It is about 25 mW/m^2, which is comparable with what has been estimated from more direct measurements using the Chatanika radar (Wickwar et al., 1975; Vickrey et al., 1982). Compared with the previous epoch at 2340-2355 UT on July 23, U_A increased by a factor of almost 2, while U_J gained only 56%. This makes the ratio U_J/U_A drop to as low as 3, indicating again that the particle energy deposition is most important during the maximum phase of a substorm. On the other hand, the lack of similarity between the two consecutive particle heating distributions further confirms that the heating is highly variable, both spatially and temporally.

Two examples shown in the second and third panels of Figure 3 represent a period during which the energy input from the solar wind slowly wanes. The ionospheric current distributions during the period clearly reflect such a signature. In addition to the gradual reduction of the overall current intensity, the westward electrojet starts to retreat toward the morning sector, suggesting that this is the recovery phase of a substorm. The Joule heating distribution shows much more clearly the decreasing trend of the solar wind energy input. Note that the two major heating regions associated with the auroral electrojets retreated toward dayside. In contrast to the Joule heating rates, which show a steady decrease, the global particle heating rates increased momentarily, in particular, along the equatorward edge of the auroral oval in the morning sector. It suggests again that the particle heating shows more abrupt temporal variation than does the Joule dissipation. Furthermore, such an enhancement seems to relate to the release of the stored energy in the magnetotail region, since it occurred during a period of decreasing solar wind energy input. Although the heating distribution patterns are not shown in Figures 2 and 3, a similar situation has been obtained for other intervals when the solar wind energy input was decreasing, e.g., around 0700 UT on July 24.

c. 1305-1320 UT on July 24, 1983

The IMF turned sharply southward at about 1110 UT on July 24 and persisted for about two hours, maintaining a large negative B_z component of less than -10 nT. The AE(12) indices and the solar wind energy coupling function, shown in Figure 1, clearly reflect a period of relatively isolated and high energy input. The epoch at 1305-1320 UT on July 24, 1983, shown as the last

example in Figure 3, seems to represent the maximum phase of an intense substorm; the AE(12) index was 1303 nT. This is the most disturbed epoch during the two-day interval examined in this study. The ionospheric current distribution shows the signature of the maximum phase with the well-developed westward electrojet intruded deeply into the evening sector. Although there are many fine-scale structures, the Joule heating distribution retains basically the same characteristics, i.e., the two major heating regions associated with auroral electrojets. However, one point which is unique in the cases examined in our study is that a significant Joule dissipation occurred in the midnight sector, where usually no appreciable heating was present in other cases. It can be argued that the low heating region that was previously located in the midnight sector shifted westward into the early evening sector. This shift of the minimum Joule heating region is closely associated where the region of the most intense electrojet is located.

The particle heating pattern of this epoch is highly structured, with the maximum heating region located in the evening sector. Furthermore, the region of high energy deposition is collocated with the leading edge of the westward electrojet that has intruded into the evening sector, probably closely associated with the westward traveling surge.

A comparison between the global Joule (U_J) and the particle (U_A) heating rates sheds some light on the energy deposition mode during a substorm. As would be expected from the high magnetic activity during this epoch, U_J recorded the highest rate during the entire two-day interval, while the corresponding U_A also showed a considerable increase but not the greatest one. The ratio U_J/U_A

is about 6 in this particular case, suggesting that Joule heating is the dominant energy dissipation mode, even during the maximum phase of a substorm. Recalling that particle heating is most important during the maximum phase of a substorm, we found a minimum value of 3 in the U_J/U_A ratio to occur at such a maximum of 0210-0225 UT. However, the variation in this ratio suggests that energy dissipation mechanisms may vary between substorms.

4. Statistical Analysis

Various attempts have so far been made to estimate the global Joule (U_J) and particle (U_A) heating rates, particularly in terms of one of the geomagnetic indices (Wallis and Budzinski, 1981; Nisbet, 1982; Spiro et al., 1982; Ahn et al., 1983; Baumjohann and Kamide, 1984). Such studies provide major input parameters for studies of solar wind-magnetosphere coupling (e.g., Akasofu, 1981; Baker et al., 1986) and the thermospheric dynamics (e.g., Roble and Ridley, 1987; Mazaudier et al., 1987). In the following subsections, the global Joule and particle heating rates based on the 30 available X-ray images are parameterized by the AE(12) index, and the relationship between the two heating rates is examined statistically.

a. The global Joule heating rate and the AE(12) index

This data set gives a unique opportunity to re-evaluate the expression relating U_J and the AE(12) index, since U_J calculated in this report is, for the first time, based on realistic, instantaneous, and global conductance distributions. For a total of 30 available X-ray images, a scatter diagram of the two

quantities was constructed; see Figure 4. There is a significant linearity between them. The correlation coefficient is found to be 0.90, suggesting that U_J can be estimated reasonably well from the AE(12) index. The expression relating U_J to AE(12) for one hemisphere is $U_J = 0.33$ AE(12), where U_J and AE(12) are in units of gegawatts (GW) and nanoteslas (nT), respectively. It is interesting to compare this with previous studies. Ahn et al. (1983) and Baumjohann and Kamide (1984) obtained similar relationships, i.e., $U_J = 0.23$ AE(12) and $U_J = 0.32$ AE(12), respectively. That these three results, although based on completely different conductance distributions, are quite comparable seems to support the statistically determined conductance models which were employed in the previous studies, as far as the total heating rate is concerned. Note, however, that since U_J is a globally integrated quantity, such comparability does not necessarily imply that there are also spatial similarities in the major heating regions among the Joule heating distributions resulting from different conductance models. The distribution pattern is as important as the magnitude of U_J in understanding polar ionospheric electrodynamics.

b. The global particle heating rate and the AE(12) index

Many studies have been devoted to estimating the global particle heating rate (U_A), particularly as a functional form of geomagnetic indices. For this purpose, satellite particle measurement data have been widely used. Unfortunately, a satellite provides particle data only along its trajectory. On the other hand, although it has a limited field of view, X-ray image data give two-dimensional information about particle precipitation, thus making it possible to obtain an "instantaneous" global particle heating distribution. For the 30 image data, the relationship between U_A and AE(12) is shown in Figure 5. There is a recognizable linearity between them, with a correlation coefficient

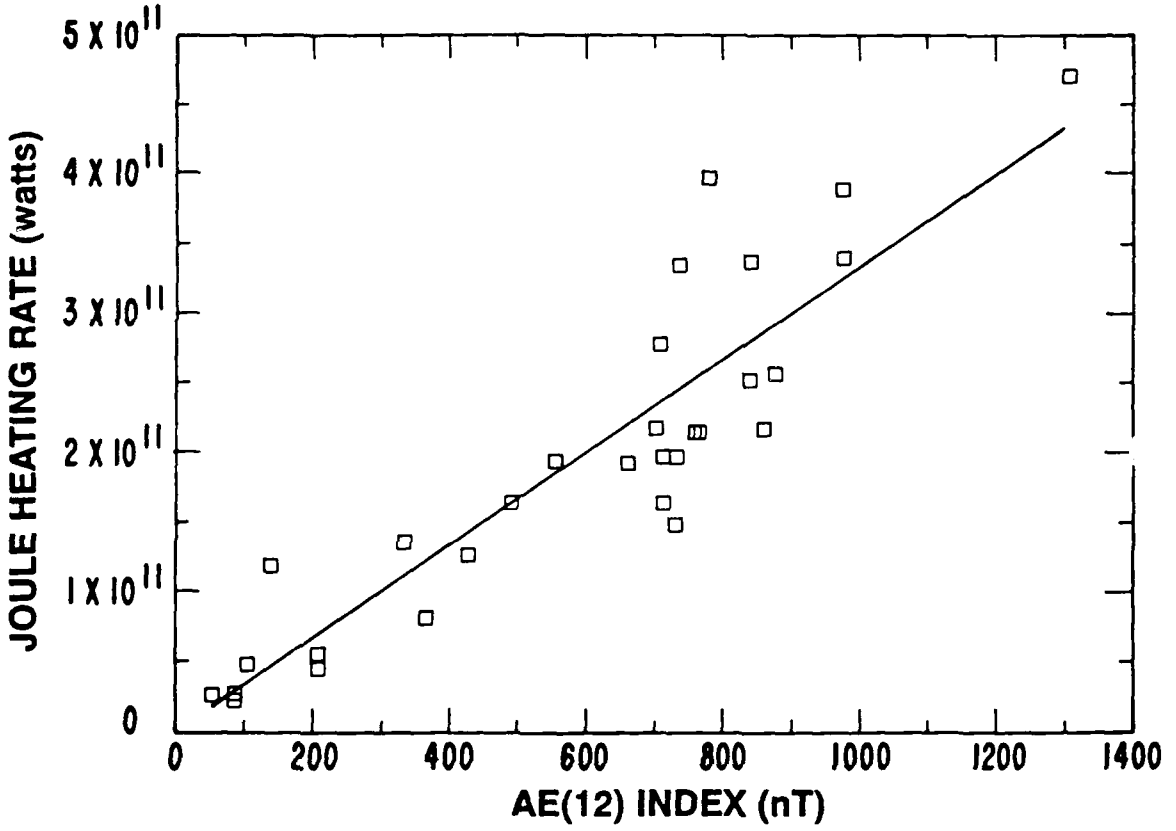

Figure 4. The Relationship Between the Global Joule Heating Rate (U_J) and the AE(12) Index

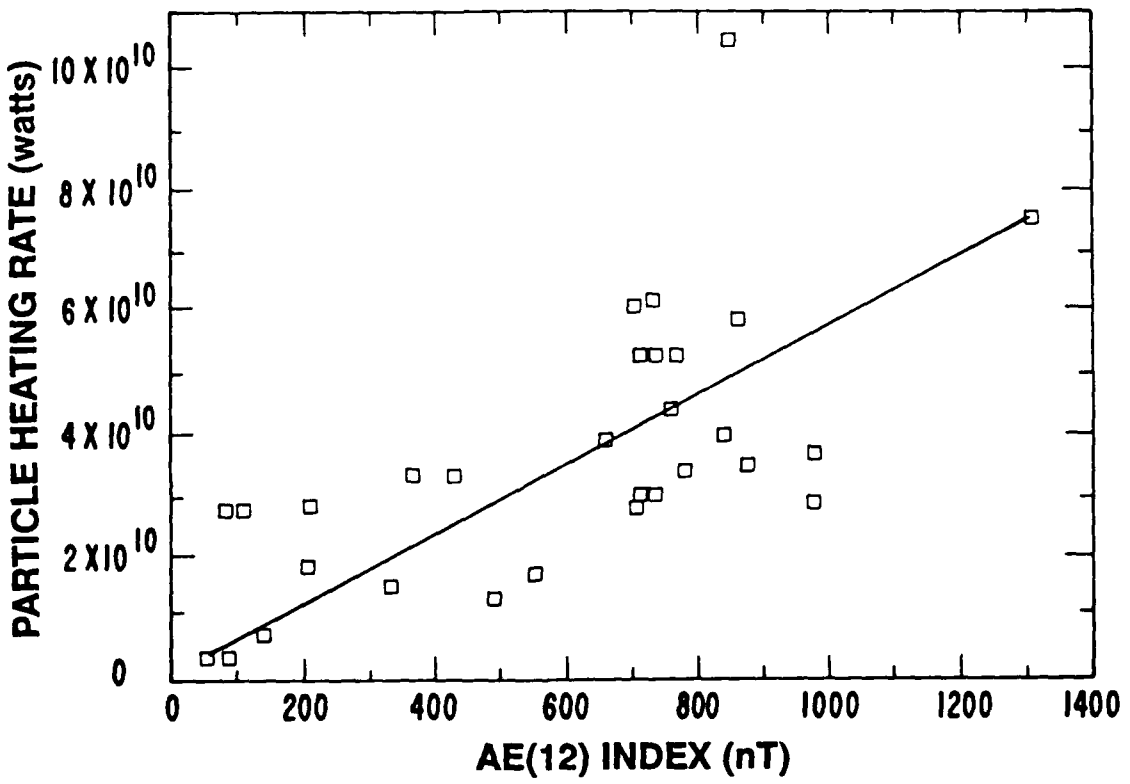

Figure 5. The Relationship Between the Global Particle Heating Rate (U_A) and the AE(12) Index

of 0.67. This indicates that the particle heating rate shows more variability than the Joule heating rate does for the same level of the geomagnetic activity. From Chatanika radar measurements, Vickrey et al. (1982) showed that both heating rates increase as the geomagnetic activity intensifies, but there is better linearity between the Joule heating rate and the electrojet current intensity than between the particle heating rate and the current intensity; see their Figure 12.

The expression relating U_A and AE(12) is obtained from Figure 5 as U_A (GW) = 0.06 AE(nT). In an effort to estimate the total energy dissipation in the magnetosphere, Akasofu (1981) introduced a similar formula, i.e., U_A = 0.1 AE(12). There are also several other studies based on satellite particle measurements. Wallis and Budzinski (1981) estimated U_A for two activity levels. For the moderate activity level expressed by the K_p index ranging from 3+ to 9, U_A was 12 GW. Although we cannot make direct comparison with the present study, their result seems to be more underestimated than the present one. Employing a similar method and data, Spiro et al. (1982) obtained another empirical formula, U_A (GW) = 0.175 AE (nT) + 16, which is larger than ours by a factor of 3 or so. Another estimation based on satellite particle data was made by Foster et al. (1986), with an introduction of the precipitation activity index ranging from 1 to 10. For example, at the level 7 corresponding to 3+ in the K_p index, U_A is about 30, and it reaches 96 GW during the maximum activity level. On the other hand, Ahn et al. (1983) devised a simple empirical formula relating the particle heating data estimated from Chatanika radar measurements with the ground horizontal magnetic disturbances. Interestingly, their formula relating U_A to AE(12) happens to be nearly exactly the same as that resulting from the present study. Recently Lummerzheim (1987) introduced a method to

estimate the two-dimensional spectral information on the precipitating particles from the DE satellite optical data. According to one example, U_A was 110 GW when AE(12) was approximately 750 nT.

c. The relationship between the Joule and particle heating rates

Figure 6 shows the relationship between U_J and U_A with the correlation coefficient of 0.52. One important point to be learned from the figure is the ratio of U_J to U_A, which has a profound implication for the energy dissipation mode in the polar ionosphere (Baker et al., 1986). According to Wickwar et al. (1975), who used Chatanika radar data, the ratio varies from about 3 to 1/4, while Vickrey et al. (1982), using the same radar measurements, concluded that the daily averages of the two energy dissipation rates are roughly equal. Unlike these studies, Figure 6 shows that on the average, U_J is larger than U_A by a factor of 6. However, several points deserve to be mentioned before these results are directly compared. First, the particle heating rate by Wickwar et al. (1975) tends to be larger than that found by Vickrey et al. (1982). This can be explained by noting that the former is based on measurements made primarily around local midnight where particle heating is dominant, while the latter is based on 24-hour synoptic measurements. Second, in comparing the result by Vickrey et al. with the present study, it should be pointed out that the radar covers a latitudinal width approximately from 62° to 68°. This leaves out a significant portion of the major Joule heating regions, which are most often located poleward of the enhanced particle heating regions, and thereby underestimates U_J. The various examples shown in Figures 2 and 3 clearly demonstrate that up to 50% of the Joule dissipation occurs north of 68° in latitude.

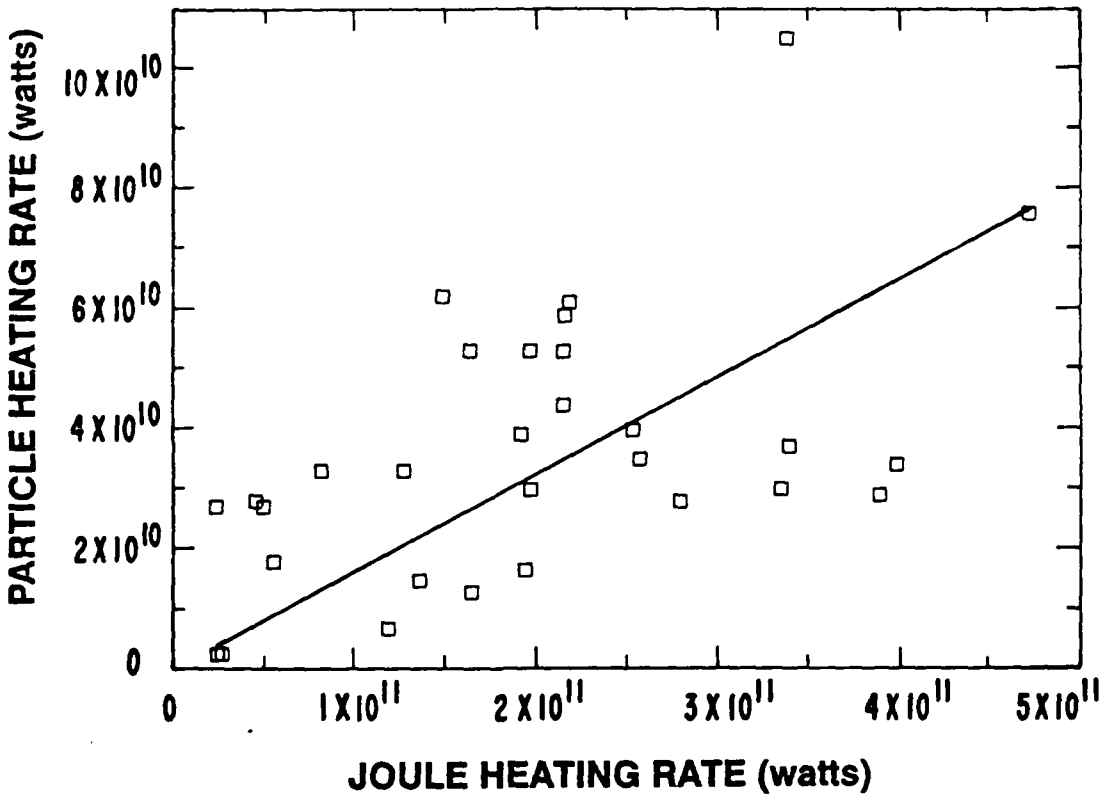

Figure 6. The Relationship Between the Global Joule (U_J) and Particle (U_A) Heating Rates

There are other observations supporting such a distribution pattern. Using the ion drift velocity and the particle precipitation observed from the AE-C satellite, Foster et al. (1983) determined statistical Joule heating distributions and confirmed that the peak input occurs between 70° and 75° in latitude during equinoctial seasons and between 65° and 75° during summer and winter; see their Figure 6. On the other hand, Rich et al. (1987) obtained the same quantity by combining data of precipitating electrons from the DMSP satellite and the simultaneously measured field-aligned currents. Their result clearly shows that the major Joule dissipation occurs around 70° or further poleward; see their Figure 3. Such studies suggest that the Chatanika radar located at 65° tends to underestimate U_J, while U_A, which occurs roughly within its field of view, is reasonably registered. Thus despite some underestimation of U_A in this study, it is quite clear that U_J is a more dominant energy source than U_A in the polar ionosphere, even during the maximum phase of substorms. The following observation further supports this conclusion. During the early phase of the substorm, starting at about 1400 UT on July 23, the satellite could not register any significant X-ray image, because the weak signal was below the threshold of the instrument, so the epochs were treated as missing data periods. If we could include such periods in our analysis, although it is not practically possible, the ratio would rise, because the moderately disturbed magnetic activity during the period must accompany considerable Joule dissipation.

A scatter diagram of the U_J/U_A ratio and the AE index presented in Figure 7 illustrates another aspect of the heating. One can see that the range of the ratio is very wide, fluctuating by more than a factor of 10 for a given level of geomagnetic activity. The correlation coefficient between the ratio and AE is

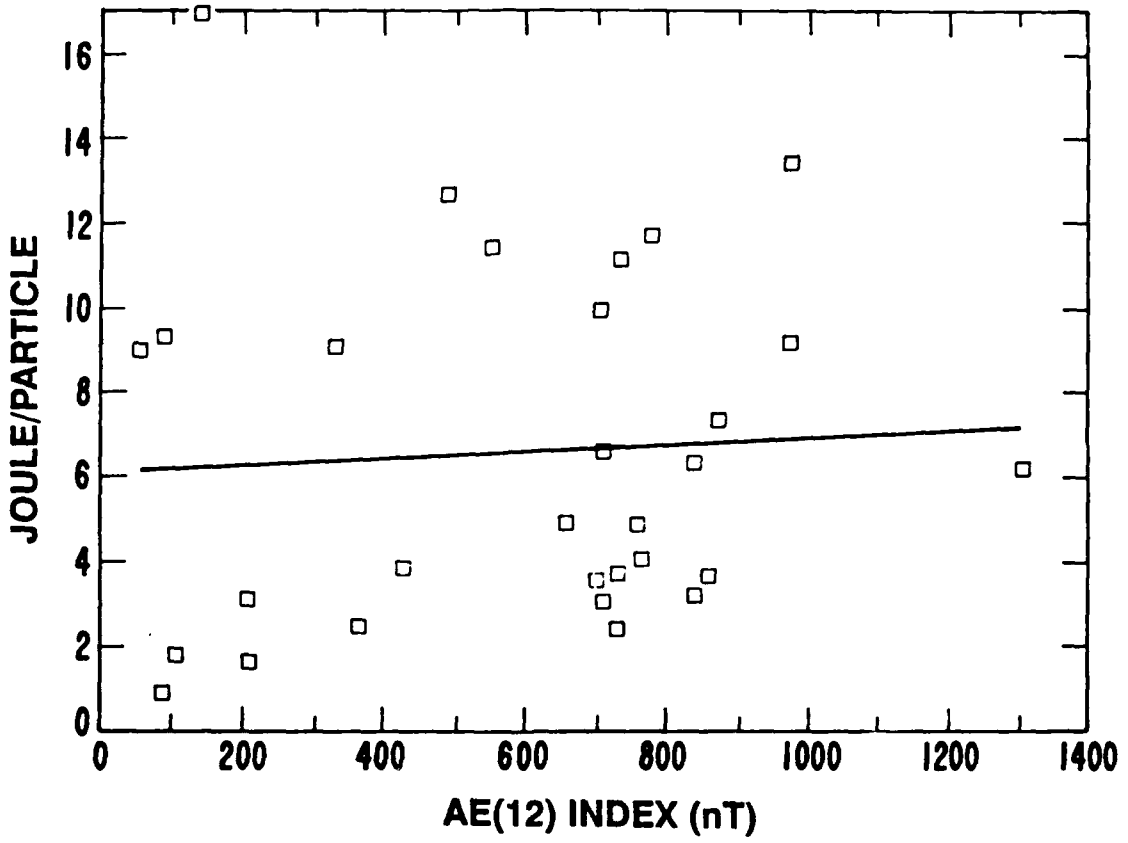

Figure 7. The Relationship Between the Ratio U_J/U_A and the AE(12) Index

found to be 0.05, indicating that there is no relationship with the AE index. The mean value of the ratio, say about 6, further suggests that the U_J is the dominant energy source. Such large fluctuations in the two-energy dissipation modes shed some light on magnetospheric processes during substorms. In examining individual epochs, it has been noticed that the two-energy dissipation mode does not seem to occur in phase; the Joule heating rate increases as magnetic activity intensifies, while the particle heating rate is significant only during the maximum phase of substorms and afterward. This may partially explain large fluctuations in the ratio, although there may be an intrinsic difference of this ratio from substorm to substorm (Wolf et al., 1986).

5. Summary and Discussion

With the advent of a method to estimate the precipitating particle parameters and, as a by-product, the ionospheric conductance distribution from bremsstrahlung X-ray image data, it is possible to obtain "instantaneous" particle and Joule heating rates incorporated with the magnetogram-inversion method. It is also important to mention that the two heating rates thus obtained are independent of one another, since the Joule heating rate was obtained by using a conductance distribution that is estimated independently from the ground magnetometer data. In an attempt to apply the new method, the two-day interval of July 23-24, 1983, has been selected, during which 30 X-ray images were available. Particular attention was paid to the spatial and temporal relationship between the two-energy dissipation modes. In spite of some shortcomings arising from the orbital characteristics of the satellite and the limitations of the instrument and measurement technique, we can summarize some prominent features of the auroral energy deposition as follows:

1. Regions of significant Joule dissipation are closely related to the auroral electrojets, with the high heating regions in the dawn and dusk sectors either extending toward the local midnight sector or shrinking back from the local noon, depending on magnetic activity. However, the local midnight or sometimes late evening sector seems to have no significant Joule dissipation, while the dayside cusp region registers a considerable heating which depends only weakly upon the magnetic activity.

2. A significantly high correlation exists between the global Joule heating rate U_J and the AE index, thus allowing us to estimate reliably the possible U_J in terms of the AE(12) index: U_J (GW) = 0.33 AE(12) for one hemisphere.

3. The particle heating tends to be more prominent during the maximum phase of a substorm and afterward than during the pre-expansion phase. Furthermore, the particle heating shows many localized structures, particularly during the maximum phase, when the maximum heating region is located at or near the local midnight sector, where the Joule heating rate is relatively unimportant.

4. Although the relationship between the global particle heating rate U_A and the AE index is less clear than that between U_J and the AE index, it still gives some idea about the contribution of U_A during substorms: U_A (GW) = 0.06 AE(12) for one hemisphere.

5. The major Joule dissipation usually occurs poleward of the major particle heating regions, particularly in the morning sector. The two heating patterns are complementary in the longitudinal direction, with the low Joule

dissipation in the local midnight made up for by the relatively strong particle heating.

6. The fact that the U_J/U_A ratio varies by more than a factor of 10 reflects the wide variability in the relative importance of the two heating rates, changing from substorm to substorm and/or from one substorm phase to another. However, the high average ratio of about 6 suggests that the auroral energy deposition during substorms is dominated by the Joule dissipation.

The relative importance of the two heating modes and their temporal behavior during substorms provides an important clue concerning the coupling between the solar wind and the magnetosphere. The global energy deposition over the polar ionosphere during the early phase of substorms, which is dominated by the Joule heating, is closely associated with the enhancement of the electric field, since the conductance enhancement during the period is generally insignificant. Thus energy seems to be dissipated primarily by a directly driven process, since the solar wind electric field controls the cross-polar cap potential difference through the dayside reconnection process (Reiff et al., 1981; Reiff and Luhmann, 1986; Schindler et al., 1987), which in turn controls the electric fields in the polar ionosphere. Furthermore, one can notice that in spite of some impulsive nature, the enhanced level of U_J in the bottom panel of Figure 1 is roughly in phase with the variation of the solar wind energy coupling function ϵ shown in the same figure, suggesting that the direct energy transfer from the solar wind to the auroral ionosphere is a dominant process. On the other hand, the global particle heating rate tends to be significant during the maximum phase of a substorm and afterward, indicating that the energy is being released explosively

from the tail region, having been stored during the pre-expansion phase. However, it should be mentioned that the enhanced particle heating rate, even during the maximum phase of a substorm and afterward, comprises only a small fraction of the total energy dissipation over the polar ionosphere.

These observations support the previous conclusion that magnetospheric substorms draw energy from both the directly driven and unloading processes (Wolf et al., 1986; Baker et al., 1986; Sauvaud et al., 1987), although the former, which is associated with U_J, is greater than the latter. Recently, through a simulation study, Lee et al. (1985) have also showed that the enhanced level of the AE index is due to direct energy transfer from the solar wind through the near-earth magnetopause to the polar atmosphere, while the impulsive changes in the AE index are the manifestation of the repeated occurrence of plasmoids.

References

Ahn, B.-H., S.-I. Akasofu, and Y. Kamide, The Joule heat production and the particle energy injection rate as a function of the geomagnetic indices of AE and AL, J. Geophys. Res., 88, 6275, 1983.

Ahn, B.-H., E. Friis-Christensen, D.J. Gorney, Y. Kamide, H.W. Kroehl, P.F. Mizera, A.D. Richmond, C.G. Sucksdorf, and C.D. Wells, Numerical modeling of polar ionospheric electrodynamics for July 23-24, 1983 utilizing ionospheric conductances deduced from DMSP X-ray images, WDC-A Report UAG-97, Boulder, CO, 1988.

Ahn, B.-H., Y. Kamide, and S.-I. Akasofu, Global ionospheric current distribution during substorms, J. Geophys. Res., 89, 1613, 1984.

Ahn, B.-H., Y. Kamide, and S.-I. Akasofu, Electrical changes of the polar ionosphere during magnetospheric substorms, J. Geophys. Res., 91, 5737, 1986.

Ahn, B.-H., H.W. Kroehl, Y. Kamide, and D.J. Gorney, Estimation of ionospheric electrodynamic parameters using ionospheric conductance deduced from bremsstrahlung X-ray image data, submitted to J. Geophys. Res., 1988.

Akasofu, S.-I., Physics of Magnetospheric Substorms, P. 81, D. Reidel, Hingham, Mass., 1977.

Akasofu, S.-I., Energy coupling between the solar wind and the magnetosphere, Space Sci. Rev., 28, 121, 1981.

Baker, D.N., L.F. Bargatze, and R.D. Zwickl, Magnetospheric response to the IMF: Substorms, J. Geomag. Geoelectr., 38, 1047, 1986.

Banks, P.M., Observations of Joule and particle heating in the auroral zone, J. Atmos. Terr. Phys., 39, 179, 1977.

Banks, P.M., J.C. Foster, and J.R. Doupnik, Chatanika radar observations relating to the latitudinal and local time variations of Joule heating, J. Geophys. Res., 86, 6869, 1981.

Baumjohann, W., and Y. Kamide, Hemispherical Joule heating and the AE indices, J. Geophys. Res., 89, 383, 1984.

Brekke, A., Electric fields, Joule and particle heating in the high latitude thermosphere, J. Atmos. Terr. Phys., 38, 887, 1976.

Foster, J.C., J.M. Holt, R.G. Musgrove, and D.S. Evans, Ionospheric convection associated with discrete levels of particle precipitation, Geophys. Res. Lett., 13, 656, 1986.

Foster, J.C., J.-P. St.-Maurice, and V.J. Abreu, Joule heating at high latitudes, J. Geophys. Res., 88, 4885, 1983.

Friis-Christensen, E., Y. Kamide, A.D. Richmond, and S. Matsushita, Interplanetary magnetic field control of high latitude electric fields and currents determined from Greenland magnetometer data, J. Geophys. Res., 90, 1325, 1985.

Fuller-Rowell, T.J., and D.S. Evans, Height integrated Pedersen and Hall conductivity patterns inferred from the TIROS-NOAA satellite data, J. Geophys. Res., 92, 7606, 1987.

Hardy, D.A., M.S. Gussenhoven, R. Raistrick, and W.J. McNeil, Statistical and functional representations of the pattern of auroral energy flux, number flux and conductivity, J. Geophys. Res., 92, 12275, 1987.

Imhof, W.L., G.H. Nakano, R.G. Johnson, and J.B. Reagan, Satellite observations of bremsstrahlung from widespread energetic electron precipitation events, J. Geophys. Res., 79, 565, 1974.

Imhof, W.L., H.D. Voss, D.W. Datlowe, and J. Mobilia, Isolated electron precipitation region at high latitudes, J. Geophys. Res., 93, 2649, 1988.

Kamide, Y., The two-component auroral electrojet, Geophys. Res. Lett., 9, 1175, 1982.

Kamide Y., J.D. Craven, L.A. Frank, B.-H. Ahn, and S.-I. Akasofu, Modeling substorm current systems using conductivity distributions inferred from DE auroral images, J. Geophys. Res., 91, 11235, 1986.

Kamide, Y., H.W. Kroehl, B.A. Hausman, R.L. McPherron, S.-I. Akasofu, P.H. Reiff, A.D. Richmond, and S. Matsushita, Numerical modeling of ionospheric parameters from global IMS magnetometer data for the CDAW-6 intervals, Rep. UAG-88, WDC-A, NOAA, Boulder, CO, 1983.

Kamide, Y., H.W. Kroehl, A.D. Richmond, B.-H. Ahn, S.-I. Akasofu, W. Baumjohann, E. Friis-Christensen, S. Matsushita, H. Maurer, G. Rostoker, R.W. Spiro, J.K. Walker, and A.Z. Zaitzev, Changes in the global electric fields and currents from March 17-19, 1978 from six IMS meridian chains of magnetometers, WDC-A Report UAG-87, Boulder, CO, 1982.

Kamide, Y., and S. Matsushita, Simulation studies of ionospheric electric fields and currents in relation to field-aligned currents, 1. Quiet periods, J. Geophys. Res., 84, 4083, 1979.

Kamide, Y., and A.D. Richmond, Ionospheric conductivity dependence of electric fields and currents estimated from ground magnetic observations, J. Geophys. Res., 87, 8331, 1982.

Kamide, Y., A.D. Richmond, and S. Matsushita, Estimation of ionospheric electric fields, ionospheric currents, and field-aligned currents from ground magnetic records, J. Geophys. Res., 86, 801, 1981.

Lee, L.C., Z.F. Fu, and S.-I. Akasofu, A simulation study of forced reconnection processes and magnetospheric storms and substorms, J. Geophys. Res., 90, 10896, 1985.

Lummerzheim, D., Electron transport and optical emissions in the aurora, Ph.D. Thesis, University of Alaska, Fairbanks, Alaska, 1987.

Mazaudier, C., A. Richmond, and D. Brinkman, On thermospheric winds produced by auroral heating during magnetic storms and associated dynamo electric fields, Ann. Geophysicae, 5A, 443, 1987.

Mizera, P.F., D.J. Gorney, and D.S. Evans, On the conjugacy of the aurora: High and low latitudes, Geophys. Res. Lett., 14, 190, 1987.

Mizera, P.F., D.J. Gorney, and J.L. Roeder, Auroral X-ray images from DMSP-F6, Geophys. Res. Lett., 11, 255, 1984.

Mizera, P.F., W.A. Kolasinski, D.J. Gorney, and J.L. Roeder, An auroral X-ray imaging spectrometer, J. Spacecraft and Rockets, 22, 514, 1985.

Mizera, P.F., J.G. Luhmann, W.A. Kolasinski, and J.B. Blake, Corrected observations of auroral arcs, electrons and X-rays from a DMSP satellite, J. Geophys. Res., 83, 5573, 1978.

Nisbet, J.S., Relations between the Birkeland currents, the auroral electrojet indices and high latitude Joule heating, J. Atmos. Terr. Phys., 44, 797, 1982.

Perreault, P., and S.-I. Akasofu, A study of geomagnetic storms, Geophys. J. R. Astron. Soc., 54, 547, 1978.

Reiff, P.H., and J.G. Luhmann, Solar wind control of the polar-cap voltage, Solar wind-magnetosphere coupling, edited by Y. Kamide and J.A. Slavin, p. 453, TERRAPUB, Tokyo, 1986.

Reiff, P.H., R.W. Spiro, and T.W. Hill, Dependence of polar cap potential drop on interplanetary parameters, J. Geophys. Res., 86, 7639, 1981.

Rich, F.J., M.S. Gussenhoven, and M.E. Greenspan, Using simultaneous particle and field observations on a low altitude satellite to estimate Joule heat energy flow into the high latitude ionosphere, Ann. Geophysicae, 5A, 527, 1987.

Richmond, A.D., Y. Kamide, B.-H. Ahn, S.-I. Akasofu, D. Alcayde, M. Blanc, O. de la Beaujardiere, D.S. Evans, J.C. Foster, E. Friis-Christensen, T.J. Fuller-Rowell, J.M. Holt, D. Knipp, H.W. Kroehl, R.P. Lepping, R.J. Pellinen, C. Senior, and A.N. Zaitzev, Mapping electrodynamic features of the high-latitude ionosphere from localized observations: Combined incoherent-scatter radar and magnetometer measurements from 1984 January 18-19, J. Geophys. Res., 93, 5760, 1988.

Robinson, R.M., R.R. Vondrak, K. Miller, T. Dabbs, and D. Hardy, On calculating ionospheric conductances from the flux and energy of precipitating electrons, J. Geophys. Res., 92, 2565, 1987.

Roble, R.G., and E.C. Ridley, An auroral model for the NCAR thermospheric general circulation model (TGCM), Ann. Geophysicae, 5A, 369, 1987.

Rosenberg, T.J., D.L. Detrick, P.F. Mizera, D.J. Gorney, F.T. Berkey, R.H. Eather, and L.J. Lanzerotti, Coordinated ground and space measurements of an auroral surge over south pole, J. Geophys. Res., 92, 11123, 1987.

Sauvaud, J.A., J.P. Treilhou, A. Saint-Marc, J. Dandouras, H. Reme, A. Korth, G. Kremser, G.K. Parks, A.N. Zaitzev, V. Petrov, L. Lazutine, and R. Pellinen, Large scale response of the magnetosphere to a southward turning of the interplanetary magnetic field, J. Geophys. Res., 92, 2365, 1987.

Schindler, K., T.E. Eastman, W.J. Heikkila, L.C. Lee, R.P. Lepping, L.R. Lyons, R.L. McPherron, and J.A. Slavin, Dialogue on the phenomenological model of substorms in the magnetotail, Magnetotail Physics, edited by A.T.Y. Lui, p. 415, The Johns Hopkins University press, Baltimore, 1987.

Spiro, R.W., P.H. Reiff, and L.J. Maher, Jr., Precipitating electron average flux and auroral zone conductances - an empirical model, J. Geophys. Res., 87, 8215, 1982.

Strickland, D.J., J.R. Jasperse, and J.A. Whalen, Dependence of auroral FUV emissions on the incident electron spectrum and neutral atmosphere, J. Geophys. Res., 88, 8051, 1983.

Vickrey, J.F., R.R. Vondrak, and S.J. Matthews, The diurnal and latitudinal variation of auroral zone ionospheric conductivity, J. Geophys. Res., 86, 65, 1981.

Vickrey, J.F., R.R. Vondrak, and S.J. Matthews, Energy deposition by precipitating particles and Joule dissipation in the auroral ionosphere, J. Geophys. Res., 87, 5184, 1982.

Wallis, D.D., and E.E. Budzinski, Empirical models of height integrated conductivities, J. Geophys. Res., 86, 125, 1981.

Wickwar, V.B., M.J. Baron, and R.D. Sears, Auroral energy input from energetic electrons and Joule heating at Chatanika, J. Geophys. Res., 80, 4364, 1975.

Wolf, R.A., S.-I. Akasofu, S.W.H. Cowley, R.L. McPherron, G. Rostoker, G.L. Siscoe, and B.U.O. Sonnerup, Coupling between the solar wind and the Earth's magnetosphere: Summary comments, Solar Wind-Magnetosphere Coupling, edited by Y. Kamide and J.A. Slavin, P. 769, TERRAPUB, Tokyo, 1986.

LABORATORY OPERATIONS

The Aerospace Corporation functions as an "architect-engineer" for national security projects, specializing in advanced military space systems. Providing research support, the corporation's Laboratory Operations conducts experimental and theoretical investigations that focus on the application of scientific and technical advances to such systems. Vital to the success of these investigations is the technical staff's wide-ranging expertise and its ability to stay current with new developments. This expertise is enhanced by a research program aimed at dealing with the many problems associated with rapidly evolving space systems. Contributing their capabilities to the research effort are these individual laboratories:

Aerophysics Laboratory: Launch vehicle and reentry fluid mechanics, heat transfer and flight dynamics; chemical and electric propulsion, propellant chemistry, chemical dynamics, environmental chemistry, trace detection; spacecraft structural mechanics, contamination, thermal and structural control; high temperature thermomechanics, gas kinetics and radiation; cw and pulsed chemical and excimer laser development including chemical kinetics, spectroscopy, optical resonators, beam control, atmospheric propagation, laser effects and countermeasures.

Chemistry and Physics Laboratory: Atmospheric chemical reactions, atmospheric optics, light scattering, state-specific chemical reactions and radiative signatures of missile plumes, sensor out-of-field-of-view rejection, applied laser spectroscopy, laser chemistry, laser optoelectronics, solar cell physics, battery electrochemistry, space vacuum and radiation effects on materials, lubrication and surface phenomena, thermionic emission, photosensitive materials and detectors, atomic frequency standards, and environmental chemistry.

Computer Science Laboratory: Program verification, program translation, performance-sensitive system design, distributed architectures for spaceborne computers, fault-tolerant computer systems, artificial intelligence, microelectronics applications, communication protocols, and computer security.

Electronics Research Laboratory: Microelectronics, solid-state device physics, compound semiconductors, radiation hardening; electro-optics, quantum electronics, solid-state lasers, optical propagation and communications; microwave semiconductor devices, microwave/millimeter wave measurements, diagnostics and radiometry, microwave/millimeter wave thermionic devices; atomic time and frequency standards; antennas, rf systems, electromagnetic propagation phenomena, space communication systems.

Materials Sciences Laboratory: Development of new materials: metals, alloys, ceramics, polymers and their composites, and new forms of carbon; nondestructive evaluation, component failure analysis and reliability; fracture mechanics and stress corrosion; analysis and evaluation of materials at cryogenic and elevated temperatures as well as in space and enemy-induced environments.

Space Sciences Laboratory: Magnetospheric, auroral and cosmic ray physics, wave-particle interactions, magnetospheric plasma waves; atmospheric and ionospheric physics, density and composition of the upper atmosphere, remote sensing using atmospheric radiation; solar physics, infrared astronomy, infrared signature analysis; effects of solar activity, magnetic storms and nuclear explosions on the earth's atmosphere, ionosphere and magnetosphere; effects of electromagnetic and particulate radiations on space systems; space instrumentation.